ADVANCED ELECTRONIC MATERIALS
www.advelectronicmat.de

A High-Performance Flexible Broadband Photodetector Based on Graphene–PTAA–Perovskite Heterojunctions

*Guigang Zhou, Rui Sun, Yan Xiao, Ghulam Abbas, and Zhengchun Peng**

Organometal halide perovskites ($CH_3NH_3PbI_{3-x}Cl_x$) have received considerable attention in the field of optoelectronics due to their strong light absorption and long carrier lifetime. However, the performance such as response speed, responsivity, and stability of such detectors still need to be improved. In this paper, a flexible photodetector (PD) composed of multilayered structure of graphene–poly[bis(4-phenyl)(2,4,6-trimethylphenyl)amine] (PTAA)–perovskite-poly(methyl methacrylate) (PMMA) is proposed. The PD can detect a wide wavelength range from ultraviolet to near infrared. The PD shows a high detectivity of ≈10^{13} Jones and a responsivity of 10^5 A W^{-1} at 360 nm. More importantly, the device also shows a high bending durability, fast response time, and good stability in air due to the protection of the PMMA layer. The facile and low-cost fabrication of the flexible perovskite-based hybrid photodetector indicates the mass production for the potential application in sensitive broadband photodetection.

1. Introduction

Photodetectors with broadband wavelength have been widely investigated in recent years due to their various applications, including digital displays, imaging sensors, optoelectronic communication, and so on. Hybrid perovskite-based devices are not only applied to photovoltaic applications such as solar cells,[1–4] but also extended to photoelectronic components, such as photodetectors,[5–6] phototransistors,[7,8] and light-emitting diodes.[9–11] For example, Hu et al. fabricated a photoconductive photodetector based on organolead triiodide perovskite thin film, with a responsivity of 3.49 A W^{-1} in the ultraviolet region and 0.49 A W^{-1} in the visible region.[5] Dong et al. demonstrated a broad wavelength device based on perovskite and its responsivity reached to 84, 203, and 242 A W^{-1} at the excitation wavelength of 350, 530, and 740 nm, respectively.[12] Among the reported hybrid perovskites, methylammonium lead halide ($CH_3NH_3PbX_3$, $X = I^-$, Br^-, Cl^-) perovskites have become promising candidates for excellent-performance photodetectors due to their broadband optical absorption coefficient,[13] tunable direct bandgaps,[14] and long carrier lifetime.[15,16] Notably, the mixed halide perovskite ($CH_3NH_3PbI_{3-x}Cl_x$) has more advantages than other halogen perovskite. The presence of chlorine provides a higher mobility and longer lifetime for carrier,[17–20] leading to a high responsivity than the nonchlorine one. However, the responsivity of perovskite-based device is still very limited due to the low electron mobility of perovskite. The mobility of pure perovskite phototransistors is 1.24 and 1.01 cm^2 (V^{-1} s^{-1}) for holes and electrons respectively,[7] which is much lower than single-layer graphene.[21] In this case, a design in which perovskite working as a source layer with good absorbance and graphene as a carrier transfer layer with high mobility is an excellent solution to overcome the shortcoming of a single-perovskite-layer-based design.

Graphene, formed by carbon atoms in a hexagonal honeycomb lattice, has excellent physical properties because of its unique structure, and it is also widely used in optoelectronic applications due to their low light absorbance (≈2.3% for single-layer graphene),[22,23] superior mechanical properties, and extremely high mobility of up to 200 000 cm^2 (V^{-1} s^{-1}) for carriers.[21] Recently, many photodetectors based on graphene–perovskite hybrid structure have been proposed.[17,24–26] For example, Lee et al. reported the graphene–perovskite hybrid device with a responsivity of 180 A W^{-1} in the visible region at a channel of 50 μm,[25] which is higher than pure perovskite devices at the conductive channel of 15 μm (up to 0.49 A W^{-1}).[5] Thus, monolayer graphene is a good candidate for free charges due to its high carrier mobility. The responsivity (1.73×10^7 A W^{-1}) of graphene–perovskite hybrid device is extremely improved with channel length decreased to 3 μm.[26] However, the costly fabrication process such as photolithography, double source vacuum vapor deposition, or electron-beam lithography is needed in preparing the narrow channel length. Meanwhile, in order to obtain higher responsivity, Xie and Yan successively designed a phototransistor with a perovskite–poly(3-hexylthiophene) (P3HT)–graphene structure with a facile fabrication process (spin-coating) and a relatively narrow conductive channel of 5 μm.[17] The obtained high responsivity of 4.3×10^9 A W^{-1} was ascribed to the significant separation of photogenerated carriers in the P3HT.[24] Compared with the double-layer graphene–perovskite heterojunction devices, the responsivity of the three-layer vertical heterojunction device is markedly improved by introducing an interface layer between

G. Zhou, Dr. R. Sun, Dr. Y. Xiao, G. Abbas, Prof. Z. Peng
Key Laboratory of Optoelectronic Devices and Systems of Ministry of Education
College of Physics and Optoelectronic Engineering
Shenzhen University
Shenzhen 518060, China
E-mail: zcpeng@szu.edu.cn

The ORCID identification number(s) for the author(s) of this article can be found under https://doi.org/10.1002/aelm.202000522.

DOI: 10.1002/aelm.202000522

the graphene and perovskite layers. However, narrow-channel length with complicated process limits the photosensitive area and hinders the practical applications of the photodetectors. Meanwhile, compared with rigid photodetector, flexible optoelectronic devices have a number of advantages including portability, wearability, and low manufacturing cost.[27,28] Considering the degradation and oxidization of perovskite in air,[29] the atmosphere stability of the device must be taken into account in applications. Furthermore, the graphene is equally sensitive to air, confirming the indispensable encapsulations.

In this paper, we report a graphene–poly[bis(4-phenyl)(2,4,6-trimethylphenyl)amine] (PTAA)–perovskite vertical heterojunction flexible photodetector coated by a poly(methyl methacrylate) (PMMA) protective layer.[30] PTAA is a kind of organic hole transfer material with a wide bandgap (from −1.8 to −5.2 eV), accelerating the hole transfer in the interface between graphene and perovskite because of the good match of HOMO energy in PTAA, and suppress the electron transfer and interfacial recombination.[4] Compare with graphene–perovskite hybrid (GP) device, the performance of graphene–PTAA–perovskite (GPP)-based with PMMA (GPPP) device is highly improved with a responsivity of 10^5 and detectivity of 10^{13} Jones at the 100 μm channel length. Benefiting from the hydrophobic and protective PMMA, our device displays a high stability in air. In addition, the low-cost and easy fabrication process of our devices promise for large scale applications in near future.

2. Results and Discussion

Structural diagrams of graphene–perovskite and graphene–PTAA–perovskite are shown in **Figure 1**a,b, respectively.

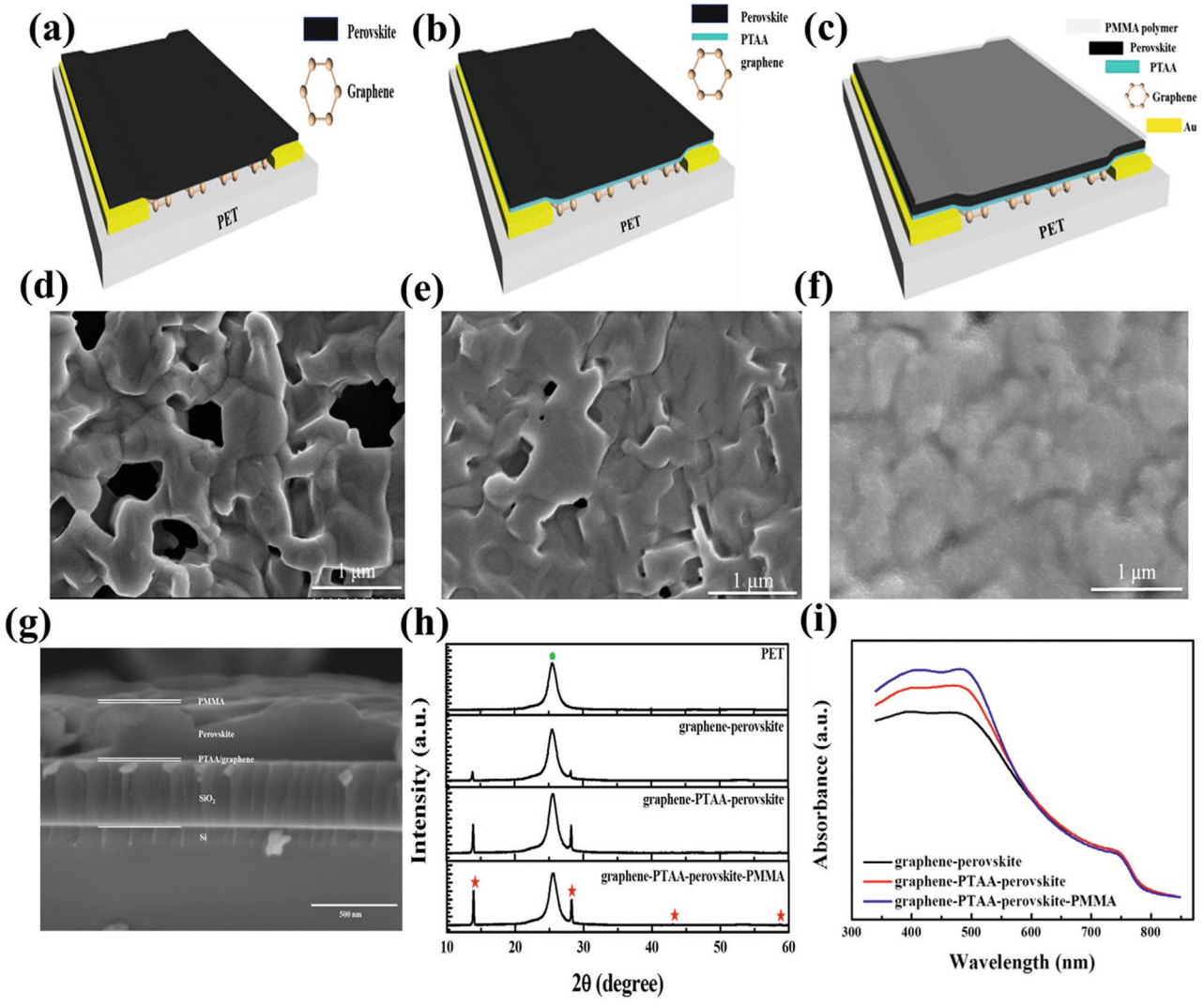

Figure 1. a) The structural diagram of the graphene–perovskite (GP) device. b) The structural diagram of the graphene–PTAA–perovskite (GPP) device. c) The structural diagram of the graphene–PTAA–perovskite–PMMA (GPPP) device. d) SEM image of the surface of the GP device. e) SEM image of the surface of the GPP device. f) SEM image of the surface of the GPPP device. g) Cross sectional SEM image of the GPPP device fabricated on a Si/SiO_2 substrate. h) XRD spectra of the GP, GPP, and GPPP devices fabricated on PET substrate. Peaks of perovskite and PET substrate are marked by red stars and a green dot, respectively. i) Absorption spectra of the GP, GPP, and GPPP devices.

Besides, a schematic diagram of a GPPP photodetector is shown in Figure 1c, where the functional layer is composed of PMMA (solvent: anisole), $CH_3NH_3PbI_{3-x}Cl_x$ perovskite, PTAA and graphene films on a flexible PET substrate. For comparison, the surface morphologies under scanning electron microscope (SEM) of the perovskite of GP, GPP, and GPPP are shown in Figure 1d–f, respectively. The perovskite film of the GP device has many pinholes on the surface (Figure 1d), while the surface morphologies of the GPP and GPPP device are more uniform (Figure 1e,f), indicating that the PTAA layer plays an important role in the homogeneity of the perovskite. Meanwhile, SEM images of those with and without anisole treatment are shown in Figure S1a,b in the Supporting Information, respectively. The uniformity of the perovskite film in the GPP device treated by anisole solvent is much better than that of the GPP device without the treatment. For SEM analysis, we used a Si/SiO_2 substrate, instead of the flexible PET substrates, to fabricate the device with the same procedure and processing parameters. Figure 1g shows the cross section of the GPPP device on Si/SiO_2 substrate. The estimated thickness of the PMMA, perovskite, and PTAA/graphene layers are 15, 300, and 20 nm, respectively. Figure 1h shows the X-ray diffraction (XRD) patterns for crystalline phases of the three different devices. The strong peaks of 14.08° and 28.43° are assigned to (110) and (220) planes of $CH_3NH_3PbI_{3-x}Cl_x$ respectively, while weak peaks at 43.04° and 58.66° is attributed to (330) and (440) planes. The results are consistent with previous reports and agrees well with the standard $CH_3NH_3PbI_{3-x}Cl_x$ spectra.[17,18,20] Furthermore, it is observed that the peaks of GPP at the (110) and (220) planes were stronger than that of GP, indicating good crystallinity of the perovskite film. Compared with those of GP and GPP device, the peaks of GPPP at the (110) and (220) planes are the strongest because of the presence of PMMA solution. To clearly understand the reason, the XRD spectrum of GPP and GPP treated with anisole is shown in Figure S1c (Supporting Information), indicating the addition of anisole solvent enhances the crystallinity of the perovskite. Figure 1i shows the absorption spectra of the GP, GPP, and GPPP devices in the UV–vis range. The absorptivity increased remarkably in the short wavelength after sandwiching a PTAA layer between the graphene and perovskite layers. The increase in absorptivity can be justified by equation $\lambda = 1240/E_g$, where E_g is the bandgap and it is 3.4 eV for PTAA. With the wavelength calculated to be ≈365 nm, an illumination of a wavelength shorter than 365 nm would increase the absorptivity of both the GPP and GPPP devices over the GP counterpart. In addition, the presence of PTAA leads to fewer pinholes in the perovskite film (Figure 1e,f), which enhance the absorbance in a broadband wavelength, including the range beyond 365 nm. To extract the effect of anisole solution, a comparison study is carried out. The absorbance spectrum of the GPP device and the GPP device treated with anisole are shown in Figure S1d (Supporting Information), indicating that anisole can enhance the absorbance in broadband light, and the absorption increases with decreasing incident wavelength. The above results demonstrate that the addition of anisole results in the reduction of crystal boundary defects that leads to crystallinity increasing and absorption intensity enhancement.

To elucidate the working mechanism of the functional device, carrier transfer diagram which reveals the transfer process of excitons (electron–hole pairs) under light illumination was displayed in **Figure 2**a. The PTAA layer works as an interfacial layer between single-layer graphene and perovskite layer, and preventing the photogenerated electrons from the perovskite to inject into the graphene film, and accelerating the injection of holes from perovskite into the graphene layer in the channel under illumination. However, excitons rapidly dissociate into holes and electrons because of ultralow exciton binding energy (35–75 meV).[31] Holes tend to diffuse into the PTAA layer and then transfer to the graphene film owing to the higher valence band level in PTAA. At the same time, free electrons must be assembled in the perovskite layer, because the lowest conduction level of PTAA is higher than the conduction level of perovskite and dielectric constant of perovskite is relatively high.[31] Therefore, the improved properties in the device are ascribed to decreased charge recombination which induced by PTAA layer. The linear photocurrent change as a function of V_{DS} under various light illuminance (illumination period: 30 s from the onset) of the 532 nm is shown in Figure 2b. The GPPP device shows excellent Ohmic contact between the graphene-PTAA bilayer films and the electrode. The sheet resistance of device is about 680 Ω according to the formula of $\rho = R^*W/L$, where R is the resistance of the device, and W/L are the width and length of the device. Furthermore, the curves of the same device along with V_{DS} under UV (360 nm) and NIR (785nm) illumination are shown in Figure S2a,b (Supporting Information). The photocurrent ΔI is given by

$$\Delta I = I_{light} - I_{dark} \tag{1}$$

where I_{light} and I_{dark} are the current of GPPP device in illumination and dark, respectively. Furthermore, the responsivity (R) can be defined as the response of photodetector against incident light. Responsivity is calculated by simply taking the ratio of photocurrent into the optical or light luminous power, as mentioned below

$$R\left(\mathrm{AW}^{-1}\right) = \frac{\Delta I}{P} \tag{2}$$

where P is the incident light luminous power. Figure 2c displays the responsivity of a GPPP device as a function of V_{DS} under varied light intensities (wavelength: 532 nm). The responsivity of the same device with UV (360 nm) and NIR (785 nm) illumination are shown in Figure S2c,d (Supporting Information). The maximum responsivity reaches to ≈10^5 A W^{-1}, which is higher than that of previously reported perovskite photodetectors.[24,25] The time-dependent photoresponse of the GPPP device under on/off illumination with multiple cycles at different wavelengths of 360, 532, 785 nm is shown in Figure 2d, indicating excellent robustness, reproducibility and short recovery time in this photodetector. However, current response under 360 nm cannot reach steady-state photocurrent under illumination for 20 s owing to the value λ (≈365 nm) of PTAA through $\lambda = 1240/E_g$. Furthermore, one cycle about the photoresponse of GPPP device (Figure 2e) is characterized by switching the light on or off at 532 nm, where current signal grows suddenly at the primary

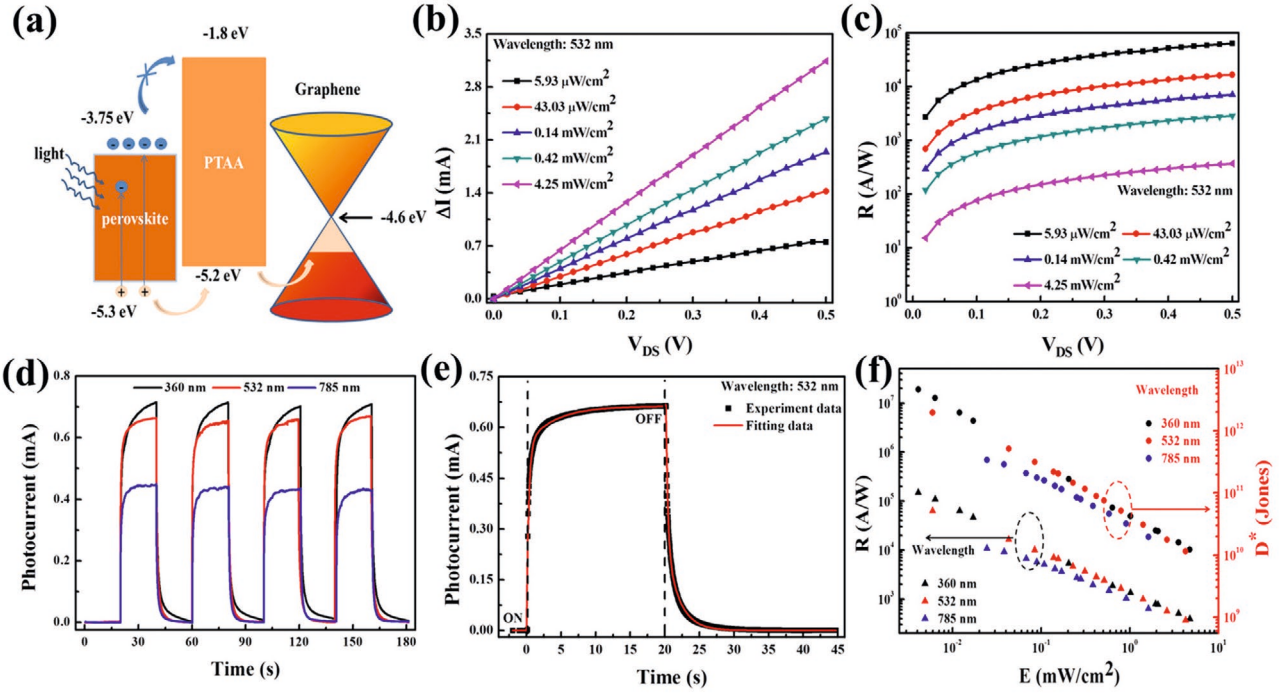

Figure 2. a) Illustration of the bandgap and carrier transfer across the vertical heterojunction of the GPP device under illumination. b) Photocurrent and c) responsivity of the GPPP device as a function of V_{DS} (0–0.5 V) under different irradiance at 532 nm. d) Time-dependent photoresponse of the GPPP device under on/off illumination at different wavelengths of 360, 532, and 785 nm (voltage: 0.1 V) with intensities of 4.74, 4.25, 1.62 mW cm^{-2}, respectively. e) Current response of the GPPP device under on/off illumination at 532 nm (4.25 mW cm^{-2}) with voltage of 0.1 V. f) The responsivity (dark ellipse) and detectivity (red ellipse) of the GPPP device as a function of different light source (360, 532, and 785 nm) at different light intensity (voltage: 0.5 V), respectively.

stage (i.e., a few hundred milliseconds) under light illumination and then increases slowly for a few minutes up to saturation. The curve of photoresponse is fitted with exponential functions, and the ascendant time–photoresponse is given by[19,25,26]

$$\Delta I_{rise} = A_1[1-\exp(-t/\tau_1)] + A_2[1-\exp(-t/\tau_2)] \quad (3)$$

where A_1 and A_2 are the magnitudes and τ_1 and τ_2 are the relaxation time constants. The τ_1 and τ_2 values for the fitted curve are 0.31 and 3.99 s, respectively. τ_1 is the time for photoinduced holes transferring from perovskite to the graphene channel, whereas τ_2 is the time for the charges transferring through the perovskite layer. Furthermore, the switch-off photoresponse in Figure 2d is fitted by[19,25,26]

$$\Delta I_{fall} = A_3 \exp(-t/\tau_3) + A_4 \exp(-t/\tau_4) \quad (4)$$

where A_3 and A_4 are magnitudes and τ_3 and τ_4 are relaxation time constants. The values of τ_3 and τ_4 from the fitted curve are 0.26 and 1.88 s, respectively. These processes are similar to those of previously reported phototransistors and photodetectors.[17–19,25,26,32] **Table 1** shows the comparison of our work and some of the previously reported works. The response time of our device is significantly shorter than that of the previously reported devices, although the responsivity and detectivity of our device are slightly compromised. During the primary stage under illumination, photoinduced holes generated from perovskite can easily transfer to graphene in the channel through PTAA layer because of the lower energy level, and therefore the current increases rapidly over time. When the hole density increases, there are more chances for holes to recombine with free electrons at the graphene–PTAA interface. The opposite electric field produced by separated charge carriers also restrained injection of holes, thus leading to a longer τ_2 and short τ_1 of the device. During the period without light, the fast decay is primarily ascribed to the recombination of accumulated electrons at the graphene–PTAA interface, while the relatively low decay may represent the long detrapping time of electrons before they transfer to the graphene layer. Notably, the response time is relatively shorter than the previously reported graphene–perovskite hybrid structure with channel length/width (3/1200 μm) fabricated by a chemical vapor deposition (CVD) method.[26] The responsivities of the GPPP at a V_{DS} of

Table 1. Comparison on the performance of our photodetector with previously reported perovskite-based photodetectors.

Reference	Length/width	R [A W^{-1}]	D^*	Rise time (τ_1)/ fall time (τ_3) [s]
17	5/800 μm	≈4.3 × 10^9	–	–
19	2/1000 μm	10^9	10^{14}	4.5/–
25	50/2000 μm	180	≈10^9	0.087/0.54
26	3/1200 μm	1.73 × 10^7	2 × 10^{15}	1.23/0.53
This work	100/2000 μm	≈10^5	≈10^{12}	0.31/0.26

0.5 V versus light irradiation at 360, 532, and 785 nm are shown in Figure 2f. Detectivity (D^*) is also a key property for photodetectors and is determined as

$$D^* = \frac{R}{\sqrt{2qj}} \tag{5}$$

where R is the responsivity of the device, q is the elementary charge, and j is the dark current intensity per unit area in the channel of device. Thence, the detectivity of the GPPP at a V_{DS} of 0.5 V at wavelengths of 360, 532, and 785 nm are also plotted in Figure 2f, and the maximum value is $\approx 10^{13}$ Jones under 360 nm illumination with the 100 µm channel length.

The effects of PMMA solution, anisole and 2,3,5,6-Tetrafluoro-7,7,8,8-tetracyanoquinodimethane (F4-TCNQ) on the photoelectric performance of device are also studied. **Figure 3**a shows a comparison between GPPP and GPP device, and the photocurrent of GPPP is higher than GPP device under the same measurement conditions, showing the PMMA solution can improve the performance. Figure 3b,c indicates the performance in the device including the PTAA layer are higher than those of the GP device without the PTAA layer, as shown in **Table 2**. Figure 3b and Table 2 show that the rise time (6.81 s) and drop time (90 s) of the GP device defined by the time taken for an 80% rise or drop in photocurrent is much higher than that of the GPP and GPPP device due to the high-density trap states in Figure 1d, leading to a long recovery time.[2] The capacitance (C) of the GP, GPP, and GPPP devices are confirmed by the actual capacitance-frequency measurement. As shown in Figure S3a (Supporting Information), the capacitance of the GP device is much higher than that of the GPP and GPPP device at low frequency range, which indicates there are fewer trap states (interface and surface trap) exist in the interior of the GPP and GPPP devices. As a result, the response speed of the GPP and GPPP devices is faster than that of GP device. The RC time constant, shown in Figure S3b (Supporting Information), of the GP device is much higher than that of the GPP and GPPP device at low frequency range. This is because the charge and discharge process of a capacitor play an essential role in the rise and recovery of the current in the photodetector.[33] These results further reveal the essential role of PTAA layer in this work to improve the response speed and performance. To further confirm the specific effect of the PTAA layer through exploring inner working mechanism, a bandgap structure diagram of the GP device is displayed on Figure S3c (Supporting Information). The excitons generated from perovskite under illumination rapidly split into electrons and holes, and all inject into graphene

Table 2. Comparison on the rise time and drop time in the GP, GPP, and GPPP devices.

Device	Rise time [s]	Drop time [s]
Graphene–perovskite	6.81	90
Graphene–PTAA–perovskite	0.65	0.78
Graphene–PTAA–perovskite–PMMA	0.86	1.28

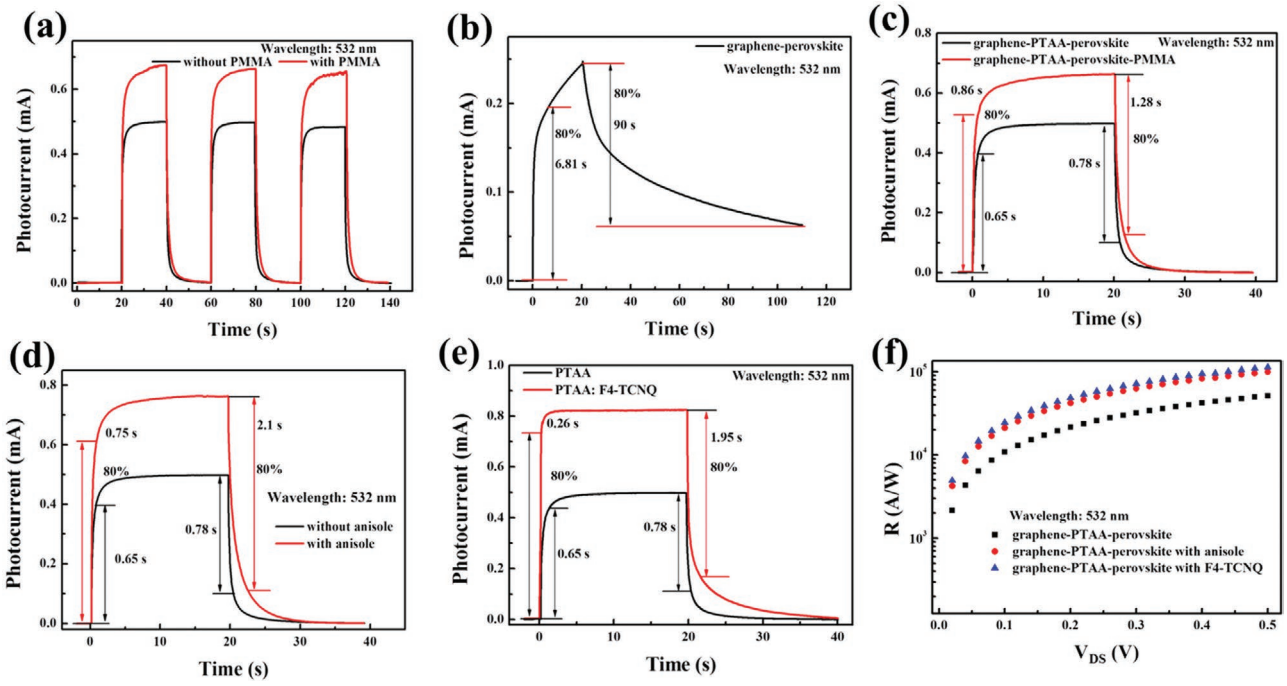

Figure 3. a) Time-dependent photoresponse of the GPP and GPPP devices as a function of I_{DS} under the same light intensity (illumination: 532 nm–4.25 mW cm^{-2}). b) Current response of the GP device to on/off illumination. V_{DS} = 0.1 V; light density (4.25 mW cm^{-2}). c) Current responses of the GPP and GPPP devices to on/off illumination. V_{DS} = 0.1 V; light density (4.25 mW cm^{-2}). d) Photoresponse of GPP device without and with anisole under periodic on/off illumination (light density: 4.25 mW cm^{-2}) at voltage of 0.1 V. e) Current responses of GPP with and without F4-TCNQ (voltage: 0.1 V; illumination: 532 nm–4.25 mW cm^{-2}). f) Responsivity of GPP device, GPP device with anisole and GPP device with F4-TCNQ as a function of V_{DS} (0–0.5 V) under same light irradiance at 532 nm (4.25 mW cm^{-2}).

because of the low energy level for holes and electrons in the graphene film, leading to lower hole concentration. According to the SEM image (Figure 1d) in GP device, high-density trap states are observed,[2] in this case the long recovery time in GP is reasonable. To further investigate the effect of anisole solvent in photoelectric property, the time-dependent response of a GPP device with and without anisole treatment are measured at 532 nm (4.25 mW cm^{-2}) with 0.1 V of V_{DS} (Figure 3d). The photocurrent of the GPP with anisole treatment is significantly enhanced compared with that of the GPP without the treatment, since anisole can lead to decrease of trap states and improve the secondary crystallinity of the perovskite.[3] The rise time of the two devices is similar; however, the drop time of the GPP device with anisole treatment (2.1 s) is longer than that of the GPP without the treatment (0.78 s). Furthermore, anisole also acts as an anti-solvent in the perovskite film formation to form a high-quality perovskite film, as previously reported.[2] The molecular structure of anisole is C_6H_5–O–CH_3, including an –O– group, two asymmetric –C_6H_5 and – CH_3 groups. Zhao et al. explained that anisole provides a hydrogen-bonding acceptor –O with lone electron pairs, which has the ability to compose hydrogen bonds C–H···O with C–H donors in *N,N*-dimethylformamide (DMF) molecule, inducing a strong intermolecular interaction between anisole solvent and DMF (solvent of perovskite solution).[34] The secondary crystallinity of perovskite in device is realized with the simultaneous evaporation of residual anisole–DMF complexes while baking since they stay as an intermediate film on the substrate during spin-coating.

To improve the performance of the GPP device, we introduce a p-doped hole transport dopant (F4-TCNQ) to the PTAA layer, in order to induce more electronic transmission channels.[4] The photocurrent generation of the GPP device with and without F4-TCNQ dopant is shown in Figure 3e. The photocurrent generated from the doped device reaches 0.825 mA, ≈60% higher than that of the undoped device. The rise time of the GPP device with F4-TCNQ dopant is 0.26 s, much shorter than that of the GPP device without the dopant (0.65 s). The drop time of the doped GPP device is slightly longer (1.95 s) than that of undoped GPP device (0.78 s). These results indicate that p-doped PTAA by F4-TCNQ can improve the performance of the GPP device. Responsivity versus V_{DS} for GPP, GPP with anisole treatment and GPP with F4-TCNQ treatment are plotted in Figure 3f. It is clear that the treatment of anisole or F4-TCNQ in GPP device improves the performance of photodetector compared to the bare GPP counterpart, and F4-TCNQ treated device shows the best responsivity for complete (0.0–0.5V) voltage interval. In addition, control device (graphene–PTAA) is also prepared. *I–V* curve of a graphene–PTAA device as a function of V_{DS} is measured at 360 nm with the highest intensity (1 μW), as plotted in Figure S3d (Supporting Information). In addition, the photocurrent of the same device is only ≈0.4 μA with the maximum light illumination under the test conditions (wavelength: 360 nm (1 μW); voltage: 0.1 V), shown in Figure S3e (Supporting Information). These results exhibit a weak absorbance in PTAA film. PTAA is an organic p-type semiconductor with a high hole mobility in the range of 10^{-3} to 10^{-2} cm^2 (V^{-1} s^{-1}),[1] which can be introduced as a substrate material for hole transport in the fabrication of devices such as perovskite solar cells[2] and organic field effect transistors.[1] Notably, the PTAA layer of all devices efficiently separates electrons and holes and prohibits charge recombination to improve device performance.

The GPPP device held in a Vernier caliper is bent with different angles in order to characterize its flexibility (**Figure 4**a). Furthermore, the mechanical strain during bending is also studied. As shown in Figure S4a (Supporting Information), the mechanical strain increases with the increase of the bending angles, and it reaches a plateau of ≈85% after ≈70°. Photoelectric performance is measured at a V_{DS} of 0.1 V under 532 nm light with 1.82 mW cm^{-2}. The photocurrent evolution after bending 100 times at various angles (10° to 70°) is shown in Figure 4b. When it is bended at 10°, the photocurrent decreased ≈40%. The change of photocurrent corresponds to the mechanical stress level at a given bending angle. The cyclic bending test at a fixed bending angle of 30° is shown in Figure 4c. After 100 cycles the photocurrent dropped from 0.6 to 0.4 mA and is relatively stable after bending 500 times. Normally, the major drawback of perovskite-based device is the instability in air,[2] owing to the easy degradation of perovskite through exposure to moisture, oxygen, and light, which limits its practical applications. To enhance the stability of the present photodetectors, effective protective layers are introduced and series of control devices are fabricated. The photographs of devices, as shown in Figure S4b (from left to right) in the Supporting Information, are GP, GPP, and GPPP, respectively. The surface color of the devices without the PMMA layer changes from black to yellow over time when stored in air, whereas the color of the device coated with a PMMA layer remains almost unchanged due to the protective of PMMA with its hydrophobic property. In addition, the transient photoresponse of the three devices is measured as a function of the exposure duration in air (voltage: 0.1 V) under periodic on/off illumination with 532 nm light, especially the storage conditions in air (temperature: 17.8 °C; relative humidity: 50%). The normalized photocurrent evolution is shown in Figure 4d. The photocurrents of the GP, GPP, and GPPP devices undergo a fast decay first and drop to 20% (less than 25 days), but the photocurrent of the devices without PMMA protective layer persistently declines with an extension of storage time in the air, meanwhile, the device with PMMA still holds 20% of its original photocurrent. To further demonstrate the effectiveness of the PMMA layer, three different devices (GPPP, GPP, and GP) are stored in air without light for 150 days and then their absorption spectra are compared in Figure 4e. The degradation rate of the devices without the PMMA layer is much faster than that of the device with the PMMA layer, which changed only slightly. These results proved that the PMMA hydrophobic layer can prevent the decay of perovskite in air.

3. Conclusion

In summary, we have fabricated a highly sensitive, stable, and broadband flexible photodetector with a vertical heterojunction (graphene–PTAA–perovskite) and a hydrophobic protective layer (PMMA). The device exhibits a high responsivity of 1×10^5 A W^{-1} and a high detectivity of 10^{13} Jones under UV–vis light illumination at a voltage of only 0.5 V even

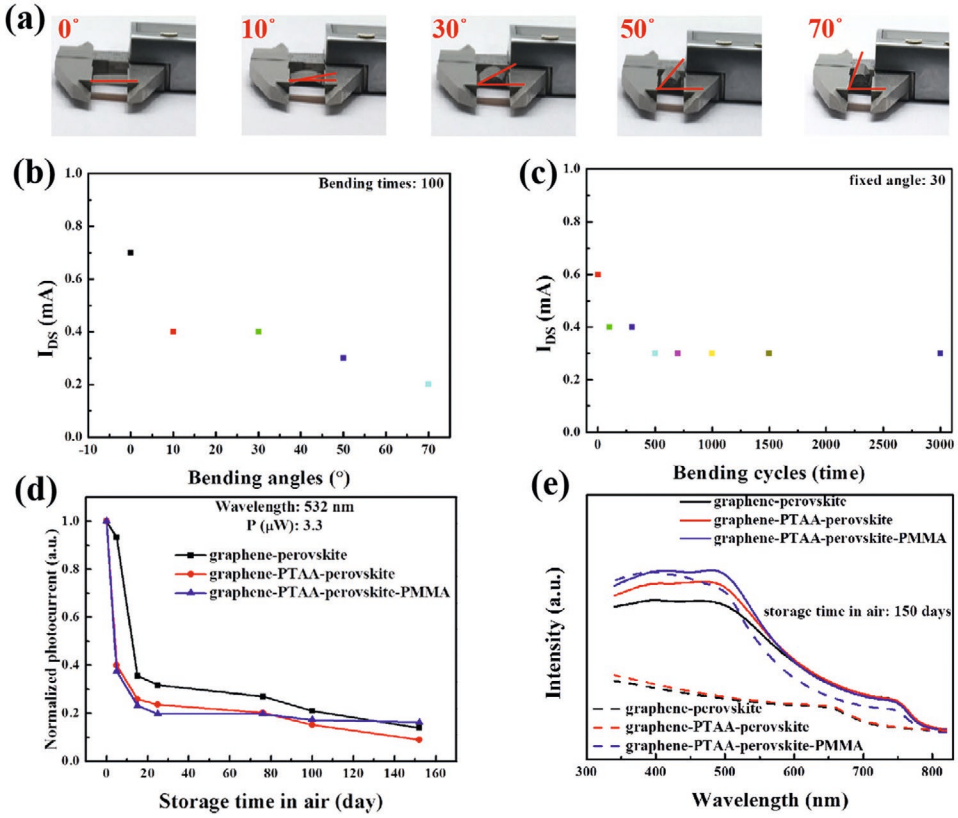

Figure 4. a) Photographs of a bended GPPP device at various bending angles. b) Evolution of photocurrent the GPPP device at various bending angles after 100 bending cycles (voltage: 0.1 V; light: 532 nm–1.82 mW cm^{-2}). c) Variation of photocurrent of the GPPP device after different bending cycles with a fixed bending angle (voltage: 0.1 V; light: 532 nm–1.82 mW cm^{-2}). d) Normalized photocurrent of the GP, GPP, and GPPP devices as a function of storage time (voltage: 0.1 V). e) Absorbance spectra of the GP, GPP, and GPPP devices in the fresh states (solid line) and 5 months later (dashed line).

with a relatively large channel length of 100 μm. The superior performance is attributed to the high mobility of graphene, intense optical absorption and long carrier lifetime of perovskite, and effective photoinduced carrier separation at the PTAA layer. The stability of the device has significantly improved by coating a PMMA film on the top surface. The high sensitivity and good stability endow our flexible photodetectors with great potential in a wide range of applications, such as digital displays, imaging sensors, optoelectronic communications, and so on.

4. Experimental Section

Materials: Single-layer graphene film was successfully fabricated on copper foil by a CVD method (6 Carbon Technology Shenzhen). The precursor solution was prepared through mixing methylammonium iodide (CH_3NH_3I) and lead chloride ($PbCl_2$) (99.5 wt%) together and dissolving them in anhydrous DMF (99.8 wt%).[17] Then, this precursor solution was filtered by a 0.22 μm PTFE membrane filter to get rid of existing particles. A 40 mg portion of PMMA crystal particles was dissolved in anisole solvent (1 mL) and heated at 50 °C for 12 h to gain a sort of completely soluble PMMA solution in a nitrogen-filled glovebox.

Device Fabrication: The PET substrates (1.5 cm × 1.5 cm) were ultrasonically washed with acetone, ethanol, and deionized water respectively. The Cr (10 nm)/Au (100 nm) electrodes were deposited by thermal evaporation with a shadow mask on top of the PET substrates. The channel length is 100 μm, while the channel width is 2 mm. Plasma irradiation treatment was applied to improve the adhesion between the depositing layer and the substrates. Single-layer graphene film was transferred onto the cleaned substrates by a wet transfer method,[23] then the PTAA layer (3 mg mL^{-1} in chlorobenzene) was spin-coated on the graphene surface at 3500 rpm for 30 s and heated at 100 °C for 20 min. The PTAA layer was treated with plasma irradiation (argon and oxygen hybrid gas) for 30 s. Then the $CH_3NH_3PbI_{3-x}Cl_x$ perovskite precursor was spin-coated onto the PTAA layer at 3500 rpm for 30 s, then the stack was annealed at 100 °C for 30 min to form the perovskite film. Finally, the PMMA solution was spin coated on the surface of the perovskite film at 3000 rpm for 30 s to obtain a protective hydrophobic PMMA layer. PET–graphene–PTAA–perovskite (GPP) and PET–graphene–perovskite (GP) devices were prepared by the same method described above. To improve the response speed of GPP device, F4-TCNQ dopants (3 wt%) was added into PTAA layer solution (3 mg mL^{-1}) to form GPP-F4-TCNQ device by using the same method.

Characterization: The absorbance spectra were characterized by PekiElmer Lambda 900. XRD measurements were performed using a Panalytical B.V. X'pertpro with Cu Kα radiation. The surface appearance of devices was measured by SEM (FEI Scios Dual Beam). Electrical characteristics of the devices were obtained by a conjugation of a Keithley 4200 semiconductor analysis device along with probe station in a glovebox filled with nitrogen. The photoelectric properties of devices were measured under illumination for 30 s every time by CHI successive lasers with 9.5 mm diameter and at a distance of 7.9 cm from laser (360, 532, and 785 nm) to device, respectively. The mechanical strain was characterized under Fatigue Stretcher (E1000, Instron). The c-f curves

were measured using the combination of a Keysight E4990A Impedance Analyzer with the Advanced Research System PSF-1-4 probe station.

Supporting Information

Supporting Information is available from the Wiley Online Library or from the author.

Acknowledgements

This work was supported by the Science and Technology Innovation Commission of Shenzhen (KQTD20170810105439418), the National Natural Science Foundation of China (61805162 and 61671308), and the Department of Education of Guangdong Province (2016KZDXM005). The authors thank Dr. Zhenhua Sun from College of Physics and Optoelectronic Engineering, Shenzhen University, for sharing his experimental equipment.

Conflict of Interest

The authors declare no conflict of interest.

Keywords

broadband wavelengths, flexible photodetectors, graphene–PTAA–perovskite heterojunctions

Received: May 21, 2020
Revised: November 30, 2020
Published online:

[1] H. Zhou, Q. Chen, G. Li, S. Luo, T. B. Song, H. S. Duan, Z. Hong, J. You, Y. Liu, Y. Yang, *Science* **2014**, *345*, 542.
[2] L. Dou, Y. M. Yang, J. You, Z. Hong, W. H. Chang, G. Li, Y. Yang, *Nat. Commun.* **2014**, *5*, 5404.
[3] Z. H. Yu, L. X. Zhang, S. Tian, F. Zhang, B. Zhang, F. F. Niu, P. J. Zeng, J. L. Qu, P. N. Rudd, J. S. Huang, J. R. Lian, *Adv. Energy Mater.* **2018**, *8*, 1701659.
[4] F. Zhang, J. Song, R. Hu, Y. R. Xiang, J. J. He, Y. Y. Hao, J. R. Lian, B. Zhang, P. J. Zeng, J. L. Qu, *Small* **2018**, *14*, 1704007.
[5] X. Hu, X. D. Zhang, L. Liang, J. Bao, S. Li, W. L. Yang, Y. Xie, *Adv. Funct. Mater.* **2014**, *24*, 7373.
[6] R. Dong, Y. Fang, J. Chae, J. Dai, Z. Xiao, Q. Dong, Y. Yuan, A. Centrone, X. C. Zeng, J. Huang, *Adv. Mater.* **2015**, *27*, 1912.
[7] F. Li, C. Ma, H. Wang, W. Hu, W. Yu, A. D. Sheikh, T. Wu, *Nat. Commun.* **2015**, *6*, 8238.
[8] Y. Chen, Y. Chu, X. Wu, W. Ou-Yang, J. Huang, *Adv. Mater.* **2017**, *29*, 1704062.
[9] Z. K. Tan, R. S. Moghaddam, M. L. Lai, P. Docampo, R. Higler, F. Deschler, M. Price, A. Sadhanala, L. M. Pazos, D. Credgington, F. Hanusch, T. Bein, H. J. Snaith, R. H. Friend, *Nat. Nanotechnol.* **2014**, *9*, 687.
[10] Y. H. Kim, H. Cho, J. H. Heo, T. S. Kim, N. Myoung, C. L. Lee, S. H. Im, T. W. Lee, *Adv. Mater.* **2015**, *27*, 1248.
[11] X. Zhang, H. Liu, W. Wang, J. Zhang, B. Xu, K. L. Karen, Y. Zheng, S. Liu, S. Chen, K. Wang, *Adv. Mater.* **2017**, *29*, 1606405.
[12] Y. Dong, Y. Gu, Y. Zou, J. Song, L. Xu, J. Li, J. Xue, X. Li, H. Zeng, *Small* **2016**, *12*, 5622.
[13] S. Kazim, M. K. Nazeeruddin, M. Gratzel, S. Ahmad, *Angew. Chem., Int. Ed.* **2014**, *53*, 2812.
[14] J. Y. Jeng, Y. F. Chiang, M. H. Lee, S. R. Peng, T. F. Guo, P. Chen, T. C. Wen, *Adv. Mater.* **2013**, *25*, 3727.
[15] S. D. Stranks, G. E. Eperon, G. Grancini, C. Menelaou, M. J. P. Alcocer, T. Leijtens, L. M. Herz, A. Petrozza, H. J. Snaith, *Science* **2013**, *342*, 341.
[16] D. Shi, V. Adinolfi, R. Comin, M. J. Yuan, E. Alarousu, A. Buin, Y. Chen, S. Hoogland, A. Rothenberger, K. Katsiev, Y. Losovyj, X. Zhang, P. A. Dowben, O. F. Mohammed, E. H. Sargent, O. M. Bakr, *Science* **2015**, *347*, 519.
[17] C. Xie, F. Yan, *ACS Appl. Mater. Interfaces* **2017**, *9*, 1569.
[18] Q. Chen, H. Zhou, Y. Fang, A. Z. Stieg, T. B. Song, H. H. Wang, X. Xu, Y. Liu, S. Lu, J. You, P. Sun, J. McKay, M. S. Goorsky, Y. Yang, *Nat. Commun.* **2015**, *6*, 7269.
[19] C. Xie, P. You, Z. Liu, L. Li, F. Yan, *Light: Sci. Appl.* **2017**, *6*, e17023.
[20] H. Yu, F. Wang, F. Xie, W. Li, N. Zhao, *Adv. Funct. Mater.* **2014**, *24*, 7102.
[21] K. S. Novoselov, A. K. Geim, S. V. Morozov, D. Jiang, Y. Zhang, S. V. Dubonos, I. V. Grigorieva, A. A. Firsov, *Science* **2004**, *306*, 666.
[22] F. Xia, T. Mueller, Y. M. Lin, A. Valdes-Garcia, P. Avouris, *Nat. Nanotechnol.* **2009**, *4*, 839.
[23] T. Mueller, F. N. A. Xia, P. Avouris, *Nat. Photonics* **2010**, *4*, 297.
[24] Y. S. Wang, Y. P. Zhang, Y. Lu, W. D. Xu, H. R. Mu, C. Y. Chen, H. Qiao, J. C. Song, S. J. Li, B. Q. Sun, Y. B. Cheng, Q. L. Bao, *Adv. Opt. Mater.* **2015**, *3*, 1389.
[25] Y. Lee, J. Kwon, E. Hwang, C. H. Ra, W. J. Yoo, J. H. Ahn, J. H. Park, J. H. Cho, *Adv. Mater.* **2015**, *27*, 41.
[26] P. H. Chang, S. Y. Liu, Y. B. Lan, Y. C. Tsai, X. Q. You, C. S. Li, K. Y. Huang, A. S. Chou, T. C. Cheng, J. K. Wang, C. I. Wu, *Sci. Rep.* **2017**, *7*, 46281.
[27] C. Xie, F. Yan, *Small* **2017**, *13*, 1701822.
[28] Q. Hua, J. Sun, H. Liu, R. Bao, R. Yu, J. Zhai, C. Pan, Z. L. Wang, *Nat. Commun.* **2018**, *9*, 244.
[29] H. Deng, X. Yang, D. Dong, B. Li, D. Yang, S. Yuan, K. Qiao, *Nano Lett.* **2015**, *15*, 7963.
[30] A. Frueh, H. J. Egelhaaf, H. Hintz, D. Quinones, C. J. Brabec, H. Peisert, *J. Mater. Res.* **2018**, *33*, 1891.
[31] M. A. Green, A. Ho-Baillie, H. J. Snaith, *Nat. Photonics* **2014**, *8*, 506.
[32] Z. L. Z. Sun, J. Li, G. A. Tai, S. P. Lau, F. Yan, *Adv. Mater.* **2012**, *24*, 1183.
[33] S. Xie, J. Yin, S. Zhang, B. Liu, W. Zhou, Z. Feng, *Solid State Electron.* **2009**, *53*, 1183.
[34] P. Zhao, B. J. Kim, X. Ren, D. G. Lee, G. J. Bang, J. B. Jeon, W. B. Kim, H. S. Jung, *Adv. Mater.* **2018**, 1802763.